THE JOURNAL OF PHYSICAL CHEMISTRY B
A JOURNAL OF THE AMERICAN CHEMICAL SOCIETY

pubs.acs.org/JPCB

Article

Vibrational Dynamics of the Intramolecular H-Bond in Acetylacetone Investigated with Transient and 2D IR Spectroscopy

Jessika L. S. Dean and Joseph A. Fournier*

Cite This: *J. Phys. Chem. B* 2022, 126, 3551−3562

Read Online

ACCESS | Metrics & More | Article Recommendations | Supporting Information

ABSTRACT: Acetylacetone (AcAc) has proven to be a fruitful but highly challenging model system for the experimental and computational interrogation of strong intramolecular hydrogen bonds. Key questions remain, however, regarding the identity of the minimum-energy structure of AcAc and the dynamics of intramolecular proton transfer. Here, we investigate the OH/OD stretch and bend regions of the enol tautomer of AcAc and its deuterated isotopologue with transient absorption and 2D IR spectroscopy. The OH bend region reveals a single dominant diagonal transition near 1625 cm^{-1} with intense cross peaks to lower-frequency modes, demonstrating highly mixed fingerprint transitions that contain OH bend character. The anharmonic coupling of the OH bend results in a highly elongated OH bend excited-state absorption transition that indicates a large manifold of OH bend overtone/combination bands in the OH stretch region that leads to strong bend−stretch Fermi resonance interactions. The OH and OD stretch regions consist of broad ground-state bleach signals, but there is no clear evidence of ω_{21} excited-state absorptions due to rapid population relaxation arising from strong intramolecular coupling to bending, fingerprint, and low-frequency H-bond modes. Orientational relaxation dynamics persist for timescales longer than the vibrational lifetimes, with polarization anisotropy components decaying within approximately 2 and 10 periods of the O−O oscillation for the OH and OD stretch, respectively. The significant isotopic dependence of the orientational dynamics is discussed in the context of intramolecular mode coupling, diffusional processes, and contributions from proton/deuteron transfer dynamics.

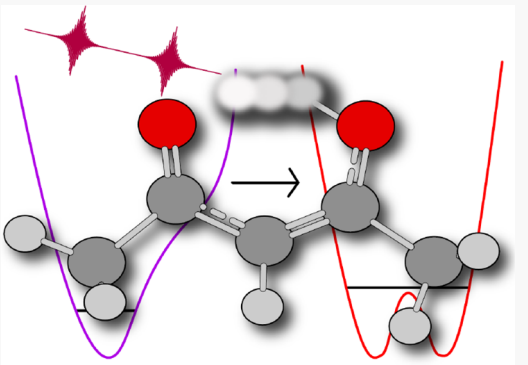

INTRODUCTION

Hydrogen bonding (H-bond) interactions are crucial components in determining structures and properties of chemical and biological systems[1−5] and are key mediators in charge transport reactions.[6−11] Owing to the high sensitivity of vibrational transitions to H-bond interactions, infrared spectroscopies provide valuable and direct insight into the properties and dynamics of H-bonds. Proton stretching transitions within strong H-bond systems, however, often manifest as broad and complex absorption features with ultrafast vibrational relaxation dynamics that are challenging to interrogate experimentally and accurately model theoretically. Recent advances in experimental ultrafast infrared spectroscopic and high-level computational methods have led to a renewed interest in unraveling the vibrational spectral signatures, energy relaxation pathways, and anharmonic mode coupling within strongly H-bonded systems.

Early seminal work by the groups of Nibbering, Hamm, and Elsaesser investigated the intramolecular H-bond in phthalic acid monomethyl ester (PMME) through the interrogation of the OH and OD stretch regions of the light and deuterated isotopologues using single-color ultrafast IR transient absorption (TA) techniques.[12−14] The most important feature observed in these spectra were strong oscillatory modulations assigned to the coherent excitation of low-frequency H-bond soft modes, the first observation of such modulations in ultrafast IR spectra. A series of studies followed, focusing on the intermolecular H-bonds formed between the homo- and heterodimers of acetic acid and nitrogen-containing species.[15−22] Two-color TA[17,23] and, later, two-dimensional infrared (2D IR) spectroscopies[21] revealed strong anharmonic coupling between the H-bonded OH/NH stretches and lower-frequency fingerprint vibrations, particularly the OH/NH bending modes. Like PMME, oscillatory modulations were observed in both diagonal and cross peaks at frequencies corresponding to intermolecular H-bond soft-mode motions that drive the strength of the H-bond interactions. In each model system, Fermi resonance interactions between the proton/deuteron stretches and overtones/combination bands of their associated bending transitions give rise to highly

Received: February 1, 2022
Revised: April 4, 2022
Published: May 10, 2022

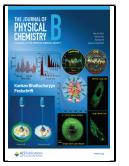

substructured lineshapes and help promote rapid population relaxation dynamics (typically <200 fs for OH/NH stretches and 300−400 fs for OD/ND stretches). Theoretical modeling by Van Hoozen and Petersen predicted the OH stretch substructure to derive from Fermi resonance interactions, while the overall spectral breadth results from low-frequency H-bond soft-mode motions, which concomitantly influence the strength of the Fermi resonances.[19,20,24] More recent studies have focused on very strong ionic intermolecular H-bond systems such as the aqueous proton[25−28] and hydrogen bifluoride anion[29] $[F\text{-}H\text{-}F]^-$, which both display vibrational signatures attributable to a highly delocalized shared proton strongly confined within steep, low-barrier proton stretch potentials.

While much progress has been made in the vibrational spectroscopic characterization of strongly H-bonded systems, the ultrafast relaxation processes of shared proton stretches that arise from the complicated interplay between Fermi resonance interactions and coupling to low-frequency soft modes has made direct interrogation and tracking of proton transfer processes and dynamics incredibly challenging experimentally. An intriguing proton transfer model system that has received much attention is acetylacetone (AcAc), a simple symmetric diketone where the enol form is energetically favored in the gas phase and low-polarity solvents due to the strong cyclic intramolecular OH−O H-bond (Figure 1a). The minimum-energy structure of AcAc, however, remains somewhat controversial. X-ray[30,31] and electron diffraction[32] experiments support an asymmetric H-bond motif corresponding to an AcAc structure with overall C_s symmetry. Microwave spectroscopy of AcAc and its ^{13}C isotopologues, on the other hand, indicated a symmetric H-bond motif with an overall C_{2v} geometry.[33] Ab initio calculations[34−40] consistently predict the C_s structure to be lowest in energy, with the C_{2v} arrangement as the proton transfer transition state. Inclusion of zero-point energies, however, make the two structures nearly isoenergetic. The highest-level calculations to date by Meuwly (CCSD(T)/cc-pVTZ) predict the C_s structure to be lower in energy by about 3.2 kcal/mol (1100 cm^{-1}) and are thus the best current estimates of the classical proton transfer barrier.[38] Inclusion of MP2 zero-point energies still favors the C_s structure but by less than 1 kcal/mol (350 cm^{-1}).

Quite recently, Meuwly[39] and Bowman[40] have independently reported full-dimensional potential energy surfaces of AcAc employing machine-learning algorithms using MP2/aug-cc-pVTZ calculations as reference data. Using their respective surfaces, Meuwly predicted the vibrational spectrum and proton residence times using classical molecular dynamics, while Bowman predicted the ground-state vibrational wavefunction and tunneling splittings using diffusion Monte Carlo simulations. Meuwly's classical simulations predicted that the majority of proton transfer events occur within 700 fs and that the transfer process is driven by the O−O proton donor−acceptor soft-mode motion. The calculated ground-state wavefunction by Bowman indicated a highly delocalized shared proton more consistent with the C_{2v} transition-state arrangement. The computed tunneling splittings were highly dependent on barrier height, ranging from 75−160 cm^{-1} for the light isotopologue (corresponding to a tunneling period ∼200−400 fs) and 20−60 cm^{-1} (∼500−1500 fs tunneling period) for deuterated AcAc, respectively.

Here, we report the ultrafast vibrational dynamics of AcAc and its doubly deuterated isotopologue (substitution of the shared and methine protons, d_2-AcAc) using TA and 2D IR spectroscopies. Strong anharmonic interactions between the OH/OD stretch, bends, other fingerprint modes, and low-frequency H-bond soft modes result in rapid intramolecular population relaxation components of all vibrational modes investigated. 2D IR spectra reveal significant mixing of the OH bend throughout the fingerprint region that results in strong Fermi resonance coupling with the OH stretch. The OH and OD stretch regions display broad bleach signals but no ω_{21} excited-state absorption signals. Curiously, the OH and OD stretch spectra do not display strong modulations at the expected O−O H-bond stretch frequency as has been observed in all other previously studied H-bond model systems. TA polarization anisotropy measurements reveal a surprisingly slow ∼1.4 ps decay component for the OD stretch, while the OH stretch anisotropy decays within ∼200 fs. We discuss the isotopic dependence of the anisotropic signals in terms of differences in proton/deuteron intramolecular transfer dynamics within the vibrational excited molecules. The data provide important new experimental benchmarks for recent high-level calculations and possible dynamical metrics and signatures of intramolecular proton transfer events.

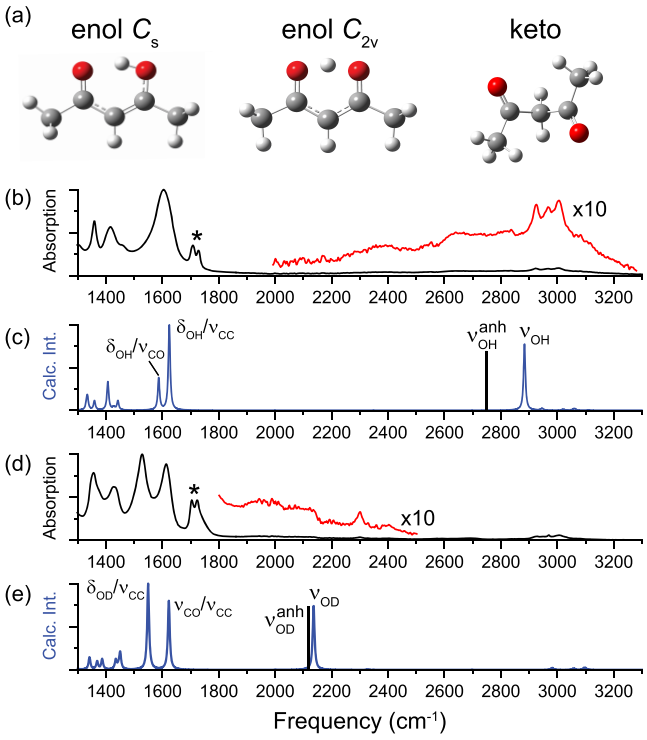

Figure 1. (a) Computed minimum-energy C_s (left) and transition-state C_{2v} (middle) structures of the enol form of AcAc. The keto form is shown on the right. (b) FTIR spectrum of neat AcAc and (c) the computed harmonic vibrational spectrum (MP2/aug-cc-pVTZ). (d) FTIR spectrum of neat d_2-AcAc and (e) the computed harmonic vibrational spectrum. The computed vibrational spectra were scaled by 0.957 and 0.969 for AcAc and d_2-AcAc, respectively. The OH and OD stretch regions are magnified for better visualization. The calculated unscaled anharmonic OH and OD stretch frequencies are indicated by the black lines in traces (c) and (e), respectively. The transitions denoted by the asterisks in (b) and (d) arise from the symmetric and antisymmetric carbonyl stretches of the keto tautomer.

https://doi.org/10.1021/acs.jpcb.2c00793
J. Phys. Chem. B 2022, 126, 3551−3562

EXPERIMENTAL METHODS

A schematic of the ultrafast IR spectrometer is presented in Supporting Information Figure S1. The output of a regenerative amplifier (Coherent Astrella, 800 nm, 30 fs, 1 kHz, 3.4 mJ/pulse) pumped a commercial optical parametric amplifier (Light Conversion, TOPAS Prime) to generate tunable near-IR signal (1.3−1.45 μm) and idler (1.8−2.1 μm) beams. The signal and idler beams were combined in a 1 mm thick $AgGaS_2$ crystal (Eksma Optics; AGS-802H) in a home-built difference frequency generation[41] setup, resulting in IR pulses tunable between 3−7 μm. IR pulse bandwidths were between 200−300 cm^{-1}, with pulse widths of about 80 fs as measured with interferometric autocorrelation.

The IR pulse was first sent through a 1 mm wedged CaF_2 window to generate a probe pulse from the reflection off the front face of the window (~1% reflection) and a reference pulse from the reflection off the wedged back face. The probe pulse was directed to a translation stage (Aerotech; ANT95L-050-MP-PL2-TAS) to control the pump-probe delay time τ_2. The reference pulse was directly routed to the MCT detector. A pump pulse pair was generated from the remaining transmitted beam in a Mach-Zehnder interferometer using two KBr beamsplitters (Spectral Systems; 945-0506H). The bright arm of the interferometer was sent to the sample, while the dark arm was actively monitored with an energy meter (Coherent; LabMax-TOP) for phase-correcting[42] of the 2D IR spectra. The fixed arm of the interferometer was mechanically chopped (Newport; model 3502) at half the repetition rate. The time delay τ_1 between the pulse pair was controlled with a second translation stage. The polarization of the pump pulses were controlled using a CdSe tunable zero-order half-wave plate (Alphalas; PO-TWP-L2−25-FIR) and ZnSe polarizer (Edmund Optics; model 62−772). The pump and probe pulses were directed and focused (~100 μm spot size) into the sample in the pump-probe geometry, generating a signal field that was self-heterodyned by the probe pulse. The probe and reference lines were dispersed by a monochromator onto a 128 × 128 pixel MCT focal-plane array detector (PhaseTech), generating the ω_3 detection axis.

For each ω_3 probe frequency at a given pump-probe delay time τ_2, the TA signal was recorded for pump pulse i as $-\log[(S_i/R_i)/(R_{i+1}/S_{i+1})]$, where S is the signal monitored by the probe and R is the reference pulse. Reported TA spectra (Figures 3 and 5) were collected at magic angle polarization with the following τ_2 step sizes: −500 to −200 fs in steps of 50 fs, −200 to 500 fs in steps of 20 fs, 550 fs to 1 ps in steps of 50 fs, and 1.2 to 8 ps in steps of 200 fs. 2D spectra were generated by monitoring the TA signal at each ω_3 pixel as a function of τ_1, the Fourier transform of which yielded the ω_1 excitation axis. All reported 2D IR spectra (Figures 2, 4, and 5) were collected at magic angle polarization. In the 6 μm region, a τ_1 step size of 4 fs was used, while a step size of 2 fs was used when pumping near 3 μm. In all experiments, τ_1 was scanned to 1200 fs for a resolution along ω_1 of 27 cm^{-1} (the free induction decays at each pixel in all regions investigated dephased rapidly within τ_1 < 400 fs). The resolution per pixel along ω_3 is about 2 cm^{-1} at 6 μm and 5 cm^{-1} at 3 μm. The τ_1 free-induction decay at each ω_3 pixel was first apodized with a Hanning window and zero-padded to twice the number of points collected for a line spacing of about 14 cm^{-1} along ω_1. The time domain data was phase-corrected using the pump spectrum collected in the dark arm of a Mach-Zehnder interferometer using the Mertz method[43] before final Fourier transformation was performed to the frequency domain. The data were interpolated to a 1 cm^{-1} spacing over ω_1 and ω_3. All 2D IR spectra are normalized to 1 with red features corresponding to ground-state bleach signals and blue features corresponding to excited-state/induced absorption signals.

For polarization anisotropy measurements, ZZZZ and ZZYY TA spectra were collected separately, making sure that pump powers and late-time TA signals were the same in both polarization schemes. Step sizes along τ_2 were as follows for AcAc: −500 to −250 fs in steps of 50 fs, −200 to 500 fs in steps of 20 fs, 550 fs to 1 ps in steps of 50 fs, and 1.2 to 12 ps in steps of 200 fs. Step sizes along τ_2 were as follows for d_2-AcAc: −500 to −250 fs in steps of 50 fs, −200 to 500 fs in steps of 20 fs, 550 fs to 1.5 ps in steps of 50 fs, and 1.6 to 8 ps in steps of 100 fs. Anisotropy was calculated as $(I_{par} - I_{perp})/(I_{par} + 2I_{perp})$.

Acetylacetone was purchased from Sigma-Aldrich and used without further purification. d_2-AcAc was synthesized following literature protocols,[44] which are briefly described in the Supporting Information. The IR spectra of both neat liquids were collected on a Bruker Alpha FTIR spectrometer in ATR mode. The TA and 2D IR spectra measured in the fingerprint region were collected from 0.7 M samples in d_{12}-cyclohexane. Samples were sandwiched between two 1 mm CaF_2 windows using a 50 μm Teflon spacer in a home-built sample cell. Due to strong background d_{12}-cyclohexane absorption near 2800 cm^{-1}, OD and OH stretch data were collected from 0.7 M samples in CCl_4 using a 300 μm Teflon spacer. Spectra measured for the neat liquids in the fingerprint region were collected by sandwiching samples between the CaF_2 windows without a spacer.

Ab initio calculations were performed with Gaussian09.[45] The optimized minimum-energy (C_s) and transition-state (C_{2v}) structures were computed at the MP2/aug-cc-pVTZ level of theory and basis set with tight convergence criteria. Harmonic frequency calculations were scaled by 0.957 for AcAc and 0.969 for d_2-AcAc to bring the OH bend (AcAc) and OD bend (d_2-AcAc) in line with the experimentally observed transitions at 1625 and 1525 cm^{-1}, respectively. Energy scans of the OH bond length discussed in the main text were performed at the B3LYP/6−311++G(d,p) level of theory and basis set. Anharmonic VPT2 calculations were performed at the MP2/6−311++G(d,p) level and basis set. Tables S1−S3 summarizing the anharmonic predictions are provided in the Supporting Information.

RESULTS AND DISCUSSION

Overview of Infrared and Computational Spectra. FTIR spectra for neat AcAc and d_2-AcAc are shown in Figure 1b,d, with corresponding harmonic vibrational predictions for the minimum-energy C_s structure presented in Figure 1c,e, respectively. The weak, broad, and double-humped feature spanning <2200 to >3000 cm^{-1} in AcAc is attributed to the strongly H-bonded proton stretch. The double-hump (~2400 and ~2800 cm^{-1}) structure is similar in appearance to OH stretch transitions in previously studied model systems and are attributed to bend−stretch Fermi resonance interactions.[19,24] The sizeable breadth indicates a large distribution of possible OH stretch frequencies that arise from low-frequency motions that vary the H-bond strength.[46] The very weak intensity suggests that the OH stretch oscillator strength is highly diluted over many background doorway states participating in the Fermi resonance interactions[47] in addition to the large

https://doi.org/10.1021/acs.jpcb.2c00793
J. Phys. Chem. B 2022, 126, 3551−3562

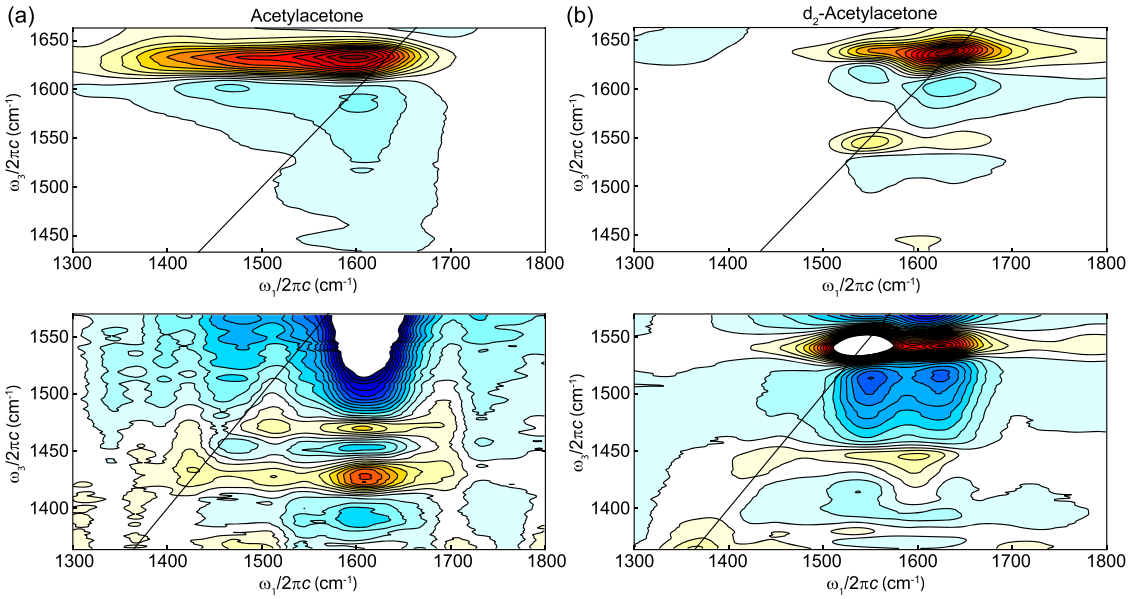

Figure 2. Isotropic 2D IR spectra collected at 150 fs waiting time for (a) AcAc and (b) d_2-AcAc with pump and probe pulses centered at 1550 cm^{-1}. The spectrum of AcAc displays a very intense cross peak band between the OH bend and other fingerprint modes in this region demonstrating strong anharmonic coupling of the OH bend throughout this spectral region. The highly extended ω_{21} transition indicates a broad manifold of OH bend-derived overtone/combination bands in the OH stretch region. The spectrum of d_2-AcAc shows coupling between the carbonyl stretch and OD bend transitions and weaker coupling to other modes in this region. The lower panels in (a) and (b) were collected from neat liquid samples to better show the weaker fingerprint modes and downhill cross peaks.

variation in the stretch frequency.[24,48] Upon deuteration, the OD stretch redshifts to ~2000 cm^{-1} and, while narrower compared to the OH stretch, is still quite broad and weak. The OD stretch likewise displays a double-humped substructure. These observations indicate that Fermi resonances and sensitivity to low-frequency motions persist in the heavy isotopologue.

The most intense transition for AcAc appears at 1625 cm^{-1}. Harmonic calculations predict a closely spaced pair of transitions both with highly mixed character consisting of OH bending, carbonyl stretching, and C═C stretching motions. The weaker fingerprint transitions spanning 1300−1500 cm^{-1} in AcAc are predicted to derive from various CH bending motions with significant OH bending contributions. The spectrum of d_2-AcAc shows two distinct transitions at 1525 and 1625 cm^{-1}, predicted to originate from OD bend/C═C stretch and carbonyl/C═C stretch normal modes, respectively. Numerous modes with OD bending character are predicted to occur in the 800−1000 cm^{-1} range. Calculated normal mode displacement vectors are presented in Figure S2 (AcAc) and Figure S3 (d_2-AcAc).

The pair of transitions near 1725 cm^{-1} result from the symmetric and antisymmetric carbonyl stretches of the keto tautomer. In the neat liquid, AcAc is about 81% enol form. For the solvents used in the nonlinear experiments, CCl_4 and cyclohexane, the enol form is 94 and 97%, respectively.[49,50] Keto-enol tautomerization occurs on much longer timescales than those investigated here.[51,52] Spectral and dynamic contributions due to the keto form and tautomerization, therefore, are not anticipated.

Fingerprint Region. *2D IR Spectra.* The isotropic 2D IR spectrum of AcAc in the 1300−1800 cm^{-1} region at 150 fs waiting time is presented in Figure 2a. A single dominant ω_{10} ground-state bleach (GSB) and ω_{21} excited-state absorption (ESA) pair is observed along the diagonal near (ω_1, ω_3) = 1625 cm^{-1}, and there is no evidence of two distinguishable transitions from the 2D lineshape as anticipated from the harmonic calculations (Figure 1c). It seems, therefore, that the two predicted transitions are either nearly degenerate or one mode is much more intense than the other. Although this transition(s) is expected to have highly mixed character and significant contribution from the carbonyl stretch, for simplicity, we will hereafter refer to the 1625 cm^{-1} transition in AcAc as the OH bend. The GSB and ESA lineshapes show no inhomogeneous broadening, indicating rapid spectral diffusion dynamics. A very intense uphill cross peak band is observed at (ω_1, ω_3) = (<1300−1550 cm^{-1}, 1625 cm^{-1}). Downhill cross peaks are also observed but are obscured by the highly elongated OH bend diagonal ESA transition. Spectra collected to 1350 cm^{-1} along the probe axis for neat liquid samples are presented in the lower panels of Figure 2 to show the weaker fingerprint modes and downhill cross peaks in more detail. The appearance of the very strong cross peak band at the earliest waiting time demonstrates that significant anharmonic coupling exists between the OH bend and the other fingerprint modes spanning <1300−1550 cm^{-1}. The anharmonic VPT2 calculations corroborate these observations, predicting off-diagonal anharmonicities in the range of −1 to −16 cm^{-1} between nearly all modes within the 1300−1700 cm^{-1} region (Table S2).

A prominent feature in the AcAc 2D IR spectrum is the highly elongated OH bend ESA transition, which extends below 1500 cm^{-1} along the probe axis. Such an extended ESA transition indicates excitation by the probe pulse from $v = 1$ in the OH bend to a large range of overtone/combination bands in the vicinity of the OH stretch. Given the highly coupled nature of the OH bend throughout the fingerprint region, a broad manifold of OH bend background states are anticipated in the OH stretch region, which will lead to strong stretch−bend Fermi resonance interactions. Indeed, the VPT2

https://doi.org/10.1021/acs.jpcb.2c00793
J. Phys. Chem. B 2022, 126, 3551−3562

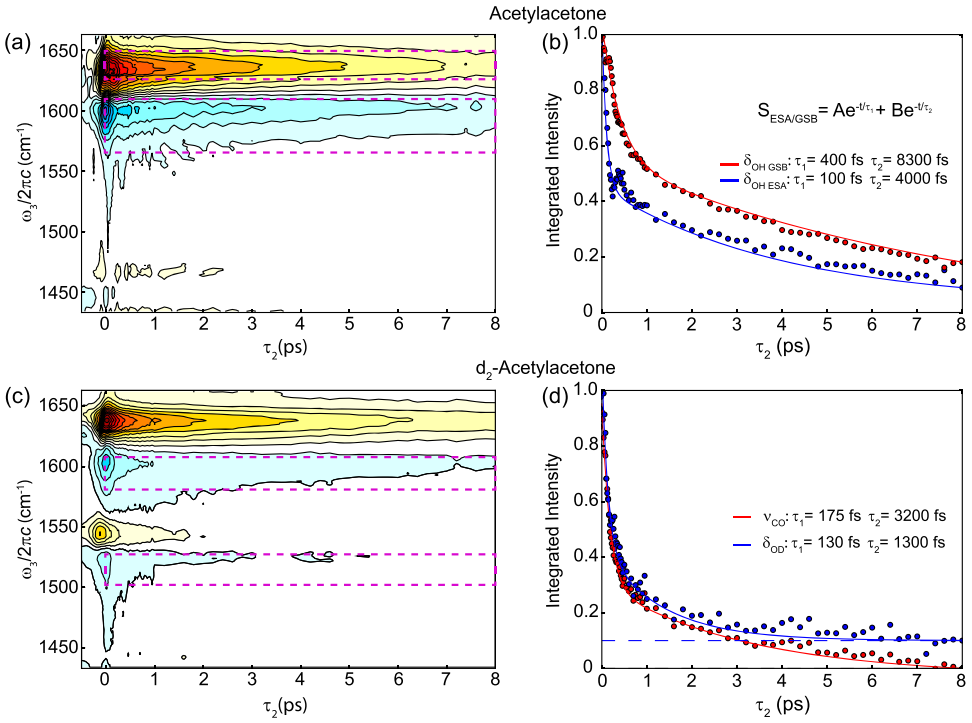

Figure 3. Isotropic TA spectra collected for (a) AcAc and (c) d_2-AcAc with pump and probe pulses centered at 1550 cm^{-1}. Relaxation dynamics are shown in (b) and (d) for AcAc and d_2-AcAc, respectively. Data were generated by integrating over the ω_3 frequencies indicated by the magenta boxes in the TA spectra. The three main transitions each show a rapid (<200 fs) initial population decay component arising from intramolecular relaxation followed by slower ps components due to intermolecular relaxation to the solvent. The decay of OD bend ESA transition in (d) is offset by 0.1 (dashed line) for better comparison.

calculations predict large cubic coupling constants (20−100 cm^{-1}) between the OH stretch and the various combination bands/overtones involving fingerprint modes that fall within the 2400−3000 cm^{-1} range (Table S3). It is also possible that the OH stretch manifold is being directly accessed by the probe pulse following excitation of the OH bend by the pump. That is, the extended tail of the ESA could correspond to direct bend-to-stretch excitation. Although such an excitation is nominally forbidden at the harmonic level, it would not be surprising given the very strong anharmonic coupling present in AcAc. A similar interpretation was given to explain the extended ESA transition observed in the bend region in neat H_2O.[53]

The 2D IR spectrum of d_2-AcAc in the same region is shown in Figure 2b. As expected from the FTIR spectrum and harmonic calculations, two main fingerprint transitions are observed in the d_2-AcAc 2D IR spectrum near 1525 and 1625 cm^{-1}. The clear splitting confirms that the single observed 1625 cm^{-1} transition in AcAc contains highly mixed OH bend and carbonyl character. For d_2-AcAc, we will refer to the 1525 cm^{-1} transition as the OD bend and the 1625 cm^{-1} transition as the carbonyl stretch. Relatively strong cross peaks between the OD bend and carbonyl stretch are present, with the VPT2 calculations predicting an off-diagonal anharmonicity constant of −12 cm^{-1} between these two modes. Cross peaks between the OD bend and carbonyl stretch to the other fingerprint modes appear much weaker to those observed in AcAc. The VPT2 calculations predict generally weaker (−1 to −5 cm^{-1}), but still significant, anharmonic constants in this region compared to AcAc, consistent with the expectation that the fingerprint modes between 1300−1500 cm^{-1} in d_2-AcAc largely derive from more localized CH bending vibrations.

Dynamics. The TA spectrum of AcAc in the fingerprint region is shown in Figure 3a. Population relaxation of the OH bend, measured from the decay of the ESA transition, shows an initial rapid decay component of ∼100 fs followed by a slow ∼4 ps decay component (Figure 3b). To aid in the interpretation of these components, the TA spectrum of the neat liquid was also collected (Figure S4). The OH bend ESA decay for the neat liquid sample displays a similarly rapid time constant that plateaus to a large offset signal that does not appreciably decay over 8 ps. We therefore interpret the fast 100 fs component observed in the solution sample to intramolecular relaxation of the OH bend via strong anharmonic couplings. The slower component then likely arises from intermolecular relaxation to the solvent. The intermolecular relaxation pathway in the neat liquid is absent since neighboring "solvent" molecules have also been excited and are vibrationally hot. The ESA decay profile also displays a damped recurrence near 400 fs. This damped oscillation likely derives from the non-rephasing cross-peak interstate coherence pathway that falls along the diagonal and oscillates at the difference frequency between the coupled transitions as a function of waiting time.[54−56] The GSB TA signal decays over even longer timescales, indicating a long-lived "hot ground state" due to low-frequency modes remaining vibrationally hot for an extended period.

The TA spectrum for d_2-AcAc is given in Figure 3c. The population relaxation dynamics of the OD bend and carbonyl stretch transitions in d_2-AcAc (Figure 3d) show qualitatively similar behavior to the OH bend dynamics: rapid intramolecular relaxation components (<200 fs) followed by slower intermolecular components (1−3 ps). The intramolecular relaxation dynamics of the OD bend and carbonyl stretch are

https://doi.org/10.1021/acs.jpcb.2c00793
J. Phys. Chem. B 2022, 126, 3551−3562

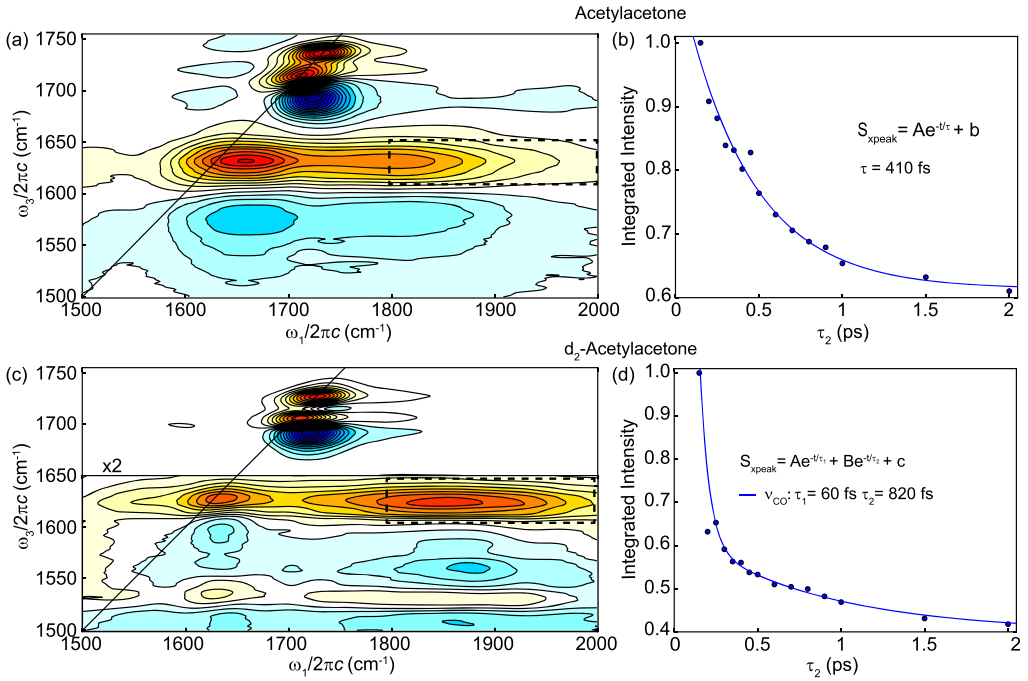

Figure 4. Isotropic 2D IR spectra collected at 150 fs waiting time for neat (a) AcAc and (c) d_2-AcAc with pump and probe pulses centered at 1800 cm^{-1}. The cross peak between the OH bend in AcAc and higher excitation frequencies are assigned to the lower-frequency tail of the OH stretch Fermi resonance doublet. In d_2-AcAc, the cross peak between the carbonyl stretch and OD bend to higher excitation frequencies are assigned to coupling with the OD stretch. Dynamics of the cross-peak bleaches are shown in (b) and (d) for AcAc and d_2-AcAc, respectively, for integration over the boxed regions in (a) and (c). The pair of strong transitions along the diagonal near 1725 cm^{-1} derive from the carbonyl stretches of the keto tautomer in the neat liquids.

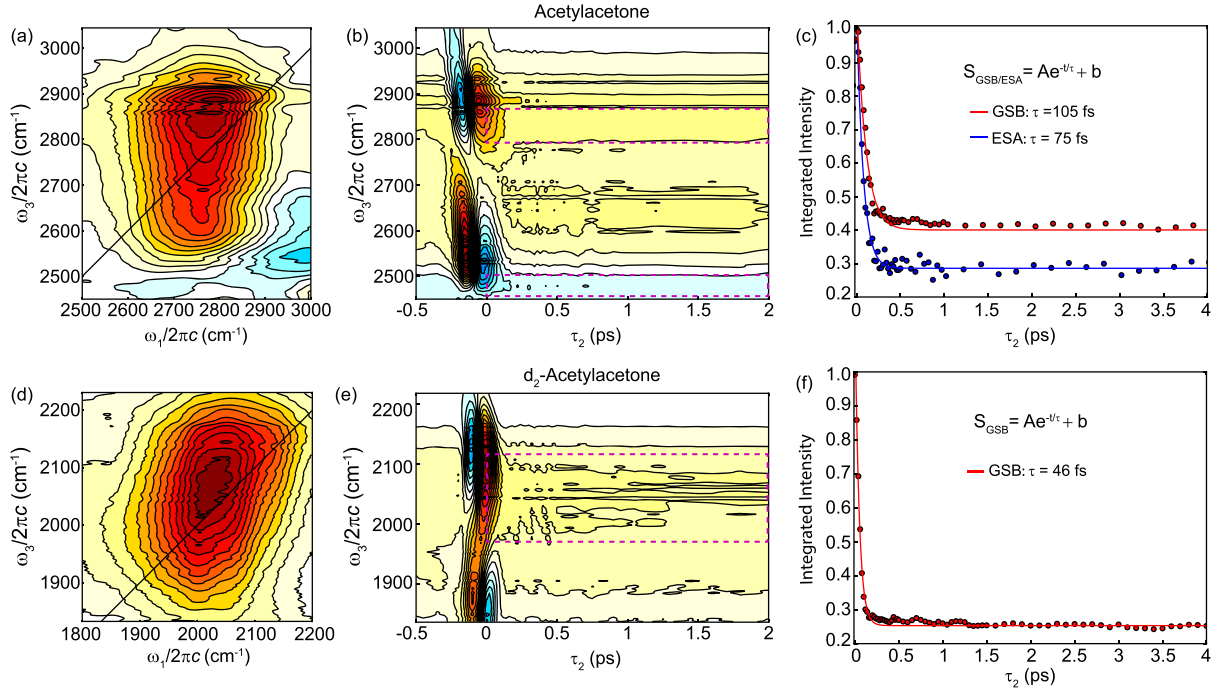

Figure 5. Isotropic 2D IR (150 fs waiting time) and TA spectra for (a, b) AcAc and (d, e) d_2-AcAc with pulses centered at 2750 cm^{-1} and 2000 cm^{-1}, respectively. The 2D IR spectra reveal broad, homogenous bleaches and no clear ω_{21} ESA transitions. Dynamics measured from the TA spectra (c, f) decay within the time resolution of the experiment to large offset signals, indicating rapid population relaxation to a long-lived hot ground state. Integrated traces in (c) and (f) correspond to the boxed regions in (b) and (e), respectively.

just as rapid as the OH bend, indicating that efficient intramolecular relaxation pathways are still present in the heavy isotopologue despite weaker experimental cross peaks and smaller predicted anharmonic constants.

For comparison, previous 2D IR measurements[57] of the symmetric and antisymmetric carbonyl stretches in the keto form of 2-aceytlcyclopentanone in CCl_4 revealed much slower population relaxation dynamics than those measured here for

https://doi.org/10.1021/acs.jpcb.2c00793
J. Phys. Chem. B 2022, 126, 3551−3562

the enol form of AcAc. The decay of the keto carbonyl stretches displayed biexponential behavior with components of ~1 and ~12 ps. The carbonyl modes in the keto form, therefore, are much more localized compared to the OH/OD bend and carbonyl stretch in enolic AcAc. These differences in dynamics between enol and keto structures demonstrates that intramolecular anharmonic couplings are greatly increased in the presence of the strong intramolecular H-bond.

Direct OH/OD Stretch−Bend Coupling. The 2D IR spectrum of d_2-AcAc in Figure 2b shows cross peaks extending from the OD bend and carbonyl stretch to higher frequencies where the OD stretch is expected. To explore this region further, 2D IR spectra were collected on neat liquid samples with the pump and probe pulses centered at 1800 cm^{-1}. These spectra are presented in Figure 3a,c for AcAc and d_2-AcAc, respectively. For d_2-AcAc, the pump pulse has sufficient bandwidth to excite the OD stretch, carbonyl stretch, and OD bend modes. Strong downhill cross peaks are observed from the OD stretch to both the carbonyl and OD bend transitions. The carbonyl stretch cross-peak dynamics (Figure 3d) shows a very rapid initial decay component, once again suggesting strong anharmonic couplings leading to fast initial intramolecular relaxation. Interestingly, a similar extended cross peak is observed in AcAc between the OH bend and pump frequencies of >1800 cm^{-1} (Figure 3a). We assign this cross peak to coupling between the OH bend and the tail of the lower-frequency OH stretch hump (Figure 1b) that manifests from the bend−stretch Fermi resonance interactions in AcAc. The slower decay dynamics of the AcAc cross peak (Figure 3b) suggests that the character of the lower-frequency OH stretch tail derives mainly from background doorway states rather than the OH stretch itself (Figure 4).

OH/OD Stretching Region. *2D IR Spectra.* Isotropic 2D IR spectra of the AcAc OH stretch and d_2-AcAc OD stretch at 150 fs waiting time are presented in Figure 5. 2D IR spectra at later waiting times are given in Figure S5 but are not appreciably different compared to the early-time spectra. Both spectra display broad GSB transitions that are homogeneously broadened within the time resolution of the experiment, indicating fast structural fluctuations that rapidly reshape the proton stretch potential and enable the sampling of all possible H-bond configurations within the excitation bandwidth. In the OH stretch spectrum (Figure 5a), bleaching signals from the CH stretching modes near ω_3 = 2900 cm^{-1} are also present. A very weak ESA feature is observed at lower probe frequencies near ω_3 = 2500 cm^{-1}. The TA spectrum (Figure 5b) shows a strong ESA transition in this probe region at early times, which could arise from a short-lived ω_{21} transition of the OH stretch. The position of the ESA within the pulse-overlap region and the strong nonresonant window response, however, does not allow us to make a definitive assignment. The small constant ESA offset signal at longer waiting times is indicative of a slight overall redshift of the OH stretch manifold arising from coupling and relaxation to lower-frequency intramolecular modes. This interpretation is consistent with the most intense ESA signal in the 2D spectrum initially occurring at higher excitation frequencies (i.e., from more weakly H-bonded OH stretches). The observed spectral shift is analogous to the "hot ground state" spectrum observed in neat H_2O and other aqueous systems[58−60] but with the key difference that relaxation into low-frequency intermolecular motions in those systems leads to a weakening of H-bonding that results in a blueshift of the water OH stretch. Similar H-bond weakening and spectral blueshifting was observed in the previously studied model H-bond systems.[13,15−17,22] We note that the early studies on PMME used pulses with much narrower (150 cm^{-1}) bandwidth, which did not allow for direct impulsive excitation of the O−O stretch but instead excited a lower-frequency out-of-plane proton bending motion that acted to break the H-bond interaction.[12−14] The unique redshift observed here for AcAc suggests a strengthening of the intramolecular H-bond upon excitation of the OH stretch and subsequent coupling/relaxation into low-frequency modes like the O−O stretch.

The OD stretch 2D IR and TA spectra are shown in Figure 5d,e, respectively. The TA shows a redshifted ESA transition at very early waiting times near 1850 cm^{-1}, although it could again arise from nonresonant window response within the pulse overlap region. Unlike the OH stretch, however, there are no persistent long-time ESA signatures resulting from a spectral shift of the OD stretch band upon intramolecular relaxation. The lack of a spectral shift ESA component suggests that the OD stretch frequency in the heavy isotopologue is less sensitive to excitation of the low-frequency H-bond soft modes.

Dynamics. The early-time ESA signal for the OH stretch decays within the time resolution (<100 fs) of the experiment, while the GSB decays within about 100 fs (Figure 5c). The GSB of the OD stretch also decays within the resolution of the experiment (Figure 5e). The extremely fast decays of the GSB and ESA transitions again point to very strong anharmonic couplings leading to rapid intramolecular population relaxation of the OH/OD stretches. The persistent GSB signals arise from relaxation into low-frequency modes (the hot ground state) instead of direct relaxation back to the overall vibrational ground state. We do not observe complete decay of GSB OH/OD stretch signals in our experiments. Decay of OH stretch GSB transitions in other model H-bond systems has been measured in the tens of ps range.[12,17,18,22]

A curious observation is the lack of oscillations in the TA spectra corresponding to coherent excitation of low-frequency H-bond modes such as the O−O stretch. Such modulations have been prominent features in all previously studied light and deuterated H-bond model systems[12,13,15−18,21,22,61] and interpreted in several ways. If an adiabatic separation of the high-frequency stretch mode and low-frequency soft modes is assumed, the pump pulse can excite from v = 0 to v = 1 in the stretch and from v = 0 in the soft mode to a superposition of soft modes within the excited stretch manifold analogous to vibronic excitation.[62−66] The superposition of soft modes, which must lie within the bandwidth of the pump pulse, generates a wavepacket on the excited-state stretch surface that gives rise to observed coherent oscillatory signals in ω_{21} ESA signals. For modulations in GSB signals, the oscillations can arise due to impulsive Raman-like excitation of the soft modes on the ground-state surface of the stretch and/or the coherent wavepacket on the excited OH/OD stretch surface that can survive relaxation to the hot ground state surface. Given the nature of the strong H-bond in AcAc, we still anticipate significant coupling between the OH/OD stretch and the O−O soft mode. The lack of such oscillations suggests that the coupled O−O excitation in AcAc undergoes rapid decoherence in comparison to previously studied H-bond model systems. We note that very weak oscillations do appear to be present in the OD stretch GSB signal for d_2-AcAc samples in d_{12}-cyclohexane solvent (Figure S6). These weak and highly

https://doi.org/10.1021/acs.jpcb.2c00793
J. Phys. Chem. B 2022, 126, 3551−3562

damped oscillations do occur at the expected period (~140 fs; ~200 cm^{-1}) of the O−O stretch.[38,39]

OH Stretch Potential. The absence of distinct ω_{21} ESA transitions, unfortunately, does not allow for a detailed characterization of the OH stretch potential. If the early-time ESA signals do, at least partially, arise from ω_{21} transitions, the diagonal anharmonicity ($2x_{ii} = \omega_{21} - \omega_{10}$) would be quite large for both the OH (≈ −300 cm^{-1}) and OD (≈ −200 cm^{-1}) stretches. We note that ω_{21} ESA signals were not clearly observed in the light isotopologues of PMME[13] or azaindole−acetic acid heterodimer[21] but did appear in d-PMME and acetic acid homodimers displaying similarly large anharmonicities.[14,22] A recent TA study on the intramolecular H-bond models 10-hydroxybenzoquinoline and 2-(2′-hydroxyphenyl)-benzothiazole using a broadband IR probe source also measured very weak early-time ESA signals assigned to ω_{21} transitions with anharmonicity ≈ −250 cm^{-1}.[61] Large anharmonicity would be in stark contrast to the "superharmonic" shared proton stretches recently characterized in the aqueous proton and HF_2^- where strong ω_{21} ESA transitions were observed at higher frequencies compared to the ω_{10} GSB transitions.[25,26,29] This behavior was attributed to steep, quartic-like proton stretch potentials of a strongly confined proton. In both cases, the zero-point energy lies above a shallow barrier resulting in a highly delocalized proton wavefunction between donor and acceptor.

Figure 6a,b shows the results of a 1D energy scan of the OH distance for the minimum-energy C_s structure and the C_{2v} transition state, respectively, with all other coordinates frozen. Indeed, the energy scan for the C_s structure yields a highly asymmetric shelf potential. Numerically solving the 1D Schrödinger equation using this potential yields the energy levels shown in Figure 6a, which predict OH and OD ω_{10} transition frequencies of 2532 and 1883 cm^{-1}, respectively. These values are lower by about 200 cm^{-1} compared with the unscaled VPT2 anharmonic predictions of 2743 and 2116 cm^{-1} for the OH and OD stretches, respectively (Figure 1c,e). The 1D surface predicts diagonal anharmonicities of −564 and −233 cm^{-1} for the OH and OD stretches, which are in reasonable agreement with the VPT2 predictions of −612 and −332 cm^{-1}, respectively. It is very possible given the large predicted anharmonicities that the spectral bandwidth of the pulses are not sufficient to capture the ω_{21} ESA transitions. The energy scan for the C_{2v} structure, however, results in a symmetric double-well potential with a shallow barrier that is qualitatively similar to the ones predicted for the aqueous proton and HF_2^- ion and the resulting energy levels display superharmonic behavior.

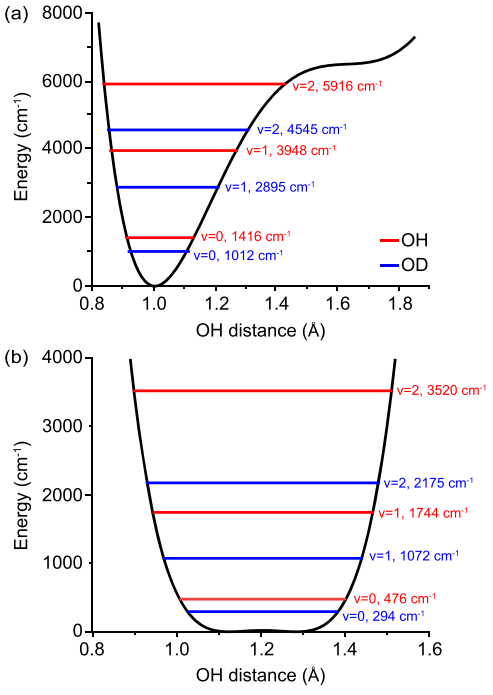

Figure 6. One-dimensional rigid energy scans of the O−H bond length for (a) the minimum-energy C_s structure and (b) the transition-state C_{2v} structure. The ω_{10} and ω_{21} transition energies predicted from the highly asymmetric C_s potential are more consistent with the observed spectra.

It is important to distinguish 1D OH stretch potentials from the multidimensional C_s−C_{2v}−C_s double-well proton transfer PES that has been the focus of most computational studies. The proton transfer surface predicts significant structural changes during the proton transfer process, including the shortening of the O−O distance from ~2.5 Å in the C_s structure to ~2.3 Å in the C_{2v} structure, equalization of the two CO bond lengths at the transition state, and rotation of the distal methyl group. Methyl group internal rotation is expected to be a low-barrier process[33,36,39] and minimally influences the 1D OH energy scans (Figure S7). Coarse 1D OH scans at various fixed O−O and CO bond lengths performed by Mavri and Grdadolnik 20 years ago[34] resulted in asymmetric potentials whenever the two CO bond lengths were held at the inequivalent C_s values, including the short 2.3 Å O−O transition-state distance. We verified these results at a higher level of theory and finer proton step size (Figure S7), which do predict slightly asymmetric potentials as well as superharmonic behavior. While the difference in the two CO bond lengths appears to be an important parameter determining the degree of asymmetry in the OH stretch potential, the O−O distance (confinement of the proton) is the main driver of anharmonic vs superharmonic behavior. 1D OH potentials are undoubtedly oversimplistic as the broad homogeneous transitions indicate a rapidly evolving distribution of structural parameters and H-bond strengths. Nevertheless, the 1D scans (slices through the proton transfer potential) offer important insight into how the key structural parameters involved in the proton transfer process influence the OH stretch potential. Importantly, the complete set of data and the general agreement of observed transitions and cross-peak patterns with the normal mode calculations for the C_s structure strongly support an asymmetric OH stretch potential typical of a highly anharmonic oscillator.

Orientational Dynamics. *Polarization Anisotropy.* TA polarization anisotropy experiments were conducted to measure the orientational dynamics of the OH and OD stretches. The anisotropy decays of the OH and OD stretches are presented in Figure 7a,b, respectively. Despite rapid population relaxation of both stretching modes within the time resolution of the experiment, the orientational relaxation dynamics occur on time scales longer than the vibrational lifetimes. The measurements were made using the GSB signals, which have long-lived hot ground state components. The hot ground state signatures of the OH/OD stretches in vibrationally hot AcAc molecules, therefore, appear to retain orienta-

https://doi.org/10.1021/acs.jpcb.2c00793
J. Phys. Chem. B 2022, 126, 3551−3562

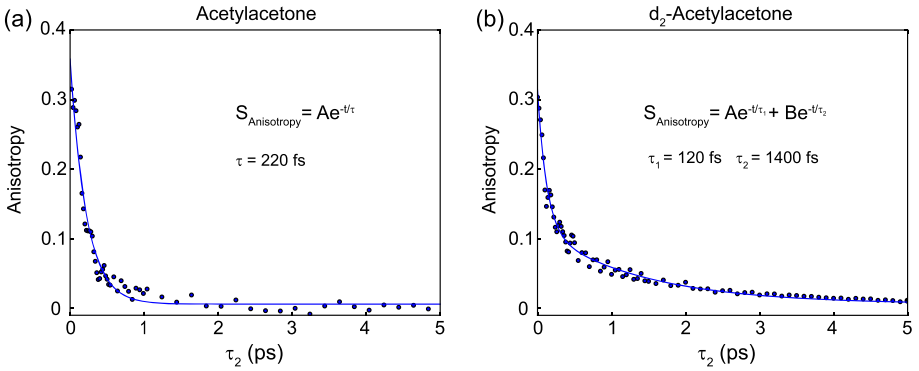

Figure 7. Polarization anisotropy dynamics for (a) the AcAc OH stretch and (b) the d_2-AcAc OD stretch. The OH stretch anisotropy decay fits best to a single exponential decay with a 220 fs time constant. The OD stretch anisotropy decay fits best to a biexponential decay with time constants of 120 fs and 1.4 ps. The fast components in each species are interpreted in terms of fast initial scrambling of the excited dipole due to strong intramolecular mode coupling. The slow component in d_2-AcAc is interpreted in terms of differences in proton/deuteron transfer dynamics of the two isotopologues on the hot ground state surface (see main text).

tional memory even with the presence of strong intramolecular anharmonic couplings and Fermi resonance mode mixing.[67,68]

The OH stretch anisotropy decay fits best to a single exponential decay with a ∼220 fs time constant, while the OD stretch anisotropy decay displays biexponential behavior with a fast ∼120 fs major component (0.65 pre-exponential amplitude) and a ∼1.4 ps minor component (0.35 amplitude). The ZZZZ and ZZYY TA spectra for both isotopologues, presented in Figure S8, also clearly show a long-lived anisotropic component in the OD stretch that is not present in the OH stretch. The fast decay components are consistent with other strongly H-bonded systems like neat water[53,58,69] and aqueous molecular ions[70,71] and interpreted in terms of rapid scrambling of the initially excited OH/OD stretch dipole due to strong anharmonic coupling with the OH/OD bends and other low-frequency modes. The strong Fermi resonance interactions also means that the OH/OD stretches cannot be considered as simple local modes but instead as a highly complicated set of transitions with significant bend/low-frequency mode character.

The slower 1.4 ps decay component in d_2-AcAc could result from diffusional dynamics. Diffusional dynamics for small molecules like AcAc, including wobbling motions and complete reorientation, typically occur in the 1−10s ps range;[72−75] the reorientation of PMME was measured to be about 20 ps.[13] Alternatively, the longer timescale could result from intermolecular relaxation processes. In aqueous hydroxide, the observed 1−5 ps anisotropic decays of the hydroxide hot ground state signals were attributed to intermolecular relaxation from initially excited hydrated hydroxide complexes to initially unexcited complexes.[67] This seems unlikely for d_2-AcAc due to much weaker solute−solvent and solvent−solvent interactions compared to the strong H-bond network in concentrated aqueous hydroxide solutions. Importantly, such stark isotopic differences in intermolecular and diffusional dynamics are not anticipated. Although diffusional dynamics and/or intermolecular relaxation processes could certainly contribute to the 1.4 ps anisotropy decay component in d_2-AcAc, they do not explain the lack of a long-time component in the light isotopologue.

The persistence of a long-lived anisotropic component in d_2-AcAc could arise from differences in the strength of intramolecular anharmonic coupling between the two isotopologues. Population relaxation dynamics, however, are not appreciably different for AcAc and d_2-AcAc. This is in contrast to the other previously studied model systems, where OD stretches decay on slower timescales (∼300−400 fs) compared to OH stretches (<200 fs) and interpreted in terms of weaker Fermi resonance interactions in the heavy isotopologue species.[13,22] While the VPT2 calculation for d_2-AcAc predicts fewer OD bend overtone/combination band background states near the OD stretch compared to AcAc, about a dozen modes with significant cubic coupling constants >30 cm^{-1} are still predicted. Finally, the anisotropy dynamics for both species display rapid initial intramolecular decay components, with the OD stretch actually having a faster initial decay. Possible alternative interpretations of the isotope-dependent anisotropy dynamics, therefore, appear warranted.

Proton and Deuteron Transfer Dynamics. The anisotropy decay components measured for the OH and OD stretches occur within the predicted[39,40] or inferred[76−78] range of timescales for intramolecular proton transfer in AcAc and related systems. Transfer of the proton/deuteron and subsequent structural rearrangement should contribute to the loss of orientational memory. The long-lived 2 ps anisotropy decay component of the aqueous proton bending mode, for example, was interpreted in terms of irreversible proton transfer following H-bond rearrangement around the aqueous proton species.[68]

For AcAc, given that the proton transfer barrier is predicted to be quite low (<350 cm^{-1}) when including zero-point energies,[38] we hypothesize that fast intramolecular vibrational relaxation of the OH stretch to the O−O stretch and other H-bond soft modes rapidly reshapes the proton transfer potential and places the vibrationally hot system near or above the proton transfer barrier. Such a scenario would result in faster tunneling dynamics and further delocalization of the proton wavefunction[40] on the hot ground state surface. Consequently, orientational memory is lost within two O−O stretch oscillation periods. The ∼200 fs timescale measured for AcAc is in good agreement with the tunneling splitting predicted by Bowman in the low-barrier limit.[40] We cannot, however, unambiguously disentangle the contributions from intramolecular coupling/mixing and proton transfer dynamics to the OH stretch anisotropy decay. Both processes are likely contributing to the orientational dynamics.

For d_2-AcAc, the OD stretch orientational memory is lost over about 10 O−O oscillation periods. The energy of the

https://doi.org/10.1021/acs.jpcb.2c00793
J. Phys. Chem. B 2022, 126, 3551−3562

vibrationally hot deuterated species, therefore, appears to lie sufficiently below the deuteron transfer barrier. Activated O−O motions are required to sample structures near the transition state that leads to deuteron transfer. The measured ∼1.4 ps timescale for d_2-AcAc is in reasonable agreement with the classical proton residence times predicted by Meuwly[39] and the tunneling splittings predicted by Bowman for deuterated AcAc.[40] Given that the orientational dynamics were measured on the OH/OD stretches on the hot ground state surface, the measured anisotropy decay times place lower limits on the average proton and deuteron transfer times in the vibrational ground state.

CONCLUSIONS

TA and 2D IR spectroscopy of acetylacetone and its deuterated isotopologue are consistent with a highly asymmetric shared proton potential deriving from predominately C_s-like structural motifs in solution. The 2D IR spectra demonstrate highly mixed OH bend character throughout the fingerprint region, resulting in a wide range of overtones and combination bands that fall within the OH stretch region and yield strong bend−stretch Fermi resonance interactions. The spectra of d_2-AcAc display similarly strong coupling between the OD stretch, OD bend, and carbonyl stretch. Although both isotopologues display equally rapid population relaxation dynamics, there are surprising isotopic differences in the orientational dynamics. We propose that the orientational dynamics of the OH and OD stretches report on differences in intramolecular proton vs deuteron transfer dynamics within the vibrationally excited molecules. The measured anisotropy decay timescales of ∼200 fs and ∼1.4 ps provide lower estimates of the proton and deuteron transfer times in the ground vibrational state and are consistent with recent high-level full-dimensional calculations. Regardless of the exact mechanism(s) for the anisotropy decay dynamics, the sizeable isotope dependence demonstrates important differences in the dynamics of the shared proton vs deuteron in acetylacetone. These significant isotopic differences are further consistent with an, on average, asymmetric structure with zero-point energies falling below the transfer barrier in the ground vibrational state. The comprehensive experimental IR spectra and ultrafast vibrational dynamics of the shared intramolecular proton/deuteron presented for acetylacetone provide critical new benchmarks for rapidly progressing computational approaches for modeling strong intramolecular H-bond interactions and proton transfer dynamics.

ASSOCIATED CONTENT

Supporting Information

The Supporting Information is available free of charge at https://pubs.acs.org/doi/10.1021/acs.jpcb.2c00793.

Synthesis of d_2-AcAc; (Tables S1−S3) anharmonic VPT2 results; (Figure S1) schematic of the ultrafast IR spectrometer; (Figure S2) calculated normal mode displacement vectors for AcAc in the fingerprint region; (Figure S3) calculated normal mode displacement vectors for d_2-AcAc in the fingerprint region; (Figure S4) TA spectra and population relaxation dynamics of neat AcAc and d_2-AcAc in the fingerprint region; (Figure S5) OH and OD stretch 2D IR spectra at longer waiting times; (Figure S6) OD stretch TA spectra of d_2-AcAc in d_{12}-cyclohexane showing weak oscillatory modulations; (Figure S7) rigid energy scans of the OH distance with distal methyl rotation and variation of the C−O distances; (Figure S8) ZZZZ and ZZYY OH/OD stretch TA spectra of AcAc and d_2-AcAc (PDF)

AUTHOR INFORMATION

Corresponding Author

Joseph A. Fournier − *Department of Chemistry, Washington University in St. Louis, St. Louis, Missouri, United States 63130*; orcid.org/0000-0001-7569-9176; Email: jfournier@wustl.edu

Author

Jessika L. S. Dean − *Department of Chemistry, Washington University in St. Louis, St. Louis, Missouri, United States 63130*

Complete contact information is available at: https://pubs.acs.org/10.1021/acs.jpcb.2c00793

Notes

The authors declare no competing financial interest.

ACKNOWLEDGMENTS

The authors gratefully acknowledge the National Science Foundation for support through a CAREER Award (CHE-2044927) and Washington University in St. Louis and the Department of Chemistry for generous startup funding.

REFERENCES

(1) Jeffrey, G. A.; Saenger, W. *Hydrogen Bonding in Biological Structures*; Springer Science & Business Media, 2012.

(2) Cleland, W. W.; Kreevoy, M. M. Low-Barrier Hydrogen Bonds and Enzymic Catalysis. *Science* **1994**, *264*, 1887−1890.

(3) Aakeröy, C. B.; Seddon, K. R. The Hydrogen Bond and Crystal Engineering. *Chem. Soc. Rev.* **1993**, *22*, 397−407.

(4) Zundel, G. *The Hydrogen Bond: Recent Developments in Theory and Experiment*; Vol. *II*, Schuster, P.; Zundel, G.; Sandorfy, C., Eds. North Holland: Amsterdam, 1976.

(5) Zundel, G. Hydrogen Bonds with Large Proton Polarizability and Proton Transfer Processes in Electrochemistry and Biology. *Adv. Chem. Phys.* **1999**, *111*, 1−217.

(6) Hibbert, F.; Emsley, J. Hydrogen Bonding and Chemical Reactivity. In *Advances in Physical Organic Chemistry*; Elsevier, 1990; Vol. *26*, pp. 255−379, DOI: 10.1016/S0065-3160(08)60047-7.

(7) Hennig, D.; Neissner, C.; Velarde, M. G.; Ebeling, W. Effect of Anharmonicity on Charge Transport in Hydrogen-Bonded Systems. *Phys. Rev. B* **2006**, *73*, No. 024306.

(8) Decornez, H.; Drukker, K.; Hammes-Schiffer, S. Solvation and Hydrogen-Bonding Effects on Proton Wires. *J. Phys. Chem. A* **1999**, *103*, 2891−2898.

(9) Decoursey, T. E. Voltage-Gated Proton Channels and Other Proton Transfer Pathways. *Physiol. Rev.* **2003**, *83*, 475−579.

(10) Schulze, B. M.; Shewmon, N. T.; Zhang, J.; Watkins, D. L.; Mudrick, J. P.; Cao, W.; Zerdan, R. B.; Quartararo, A. J.; Ghiviriga, I.; Xue, J.; et al. Consequences of Hydrogen Bonding on Molecular Organization and Charge Transport in Molecular Organic Photovoltaic Materials. *J. Mater. Chem. A* **2014**, *2*, 1541−1549.

(11) Weinberg, D. R.; Gagliardi, C. J.; Hull, J. F.; Murphy, C. F.; Kent, C. A.; Westlake, B. C.; Paul, A.; Ess, D. H.; McCafferty, D. G.; Meyer, T. J. Proton-Coupled Electron Transfer. *Chem. Rev.* **2012**, *112*, 4016−4093.

(12) Stenger, J.; Madsen, D.; Dreyer, J.; Hamm, P.; Nibbering, E. T. J.; Elsaesser, T. Femtosecond Mid-Infrared Photon Echo Study of an Intramolecular Hydrogen Bond. *Chem. Phys. Lett.* **2002**, *354*, 256−263.

(13) Madsen, D.; Stenger, J.; Dreyer, J.; Hamm, P.; Nibbering, E. T. J.; Elsaesser, T. Femtosecond Mid-Infrared Pump-Probe Study of Wave Packet Motion in a Medium-Strong Intramolecular Hydrogen Bond. *Bull. Chem. Soc. Jpn.* **2002**, *75*, 909−917.
(14) Stenger, J.; Madsen, D.; Dreyer, J.; Nibbering, E. T. J.; Hamm, P.; Elsaesser, T. Coherent Response of Hydrogen Bonds in Liquids Probed by Ultrafast Vibrational Spectroscopy. *J. Phys. Chem. A* **2001**, *105*, 2929−2932.
(15) Heyne, K.; Huse, N.; Nibbering, E. T. J.; Elsaesser, T. Coherent Vibrational Dynamics of Intermolecular Hydrogen Bonds in Acetic Acid Dimers Studied by Ultrafast Mid-Infrared Spectroscopy. *J. Phys.: Condens. Matter* **2003**, *15*, S129−S136.
(16) Heyne, K.; Huse, N.; Nibbering, E. T. J.; Elsaesser, T. Ultrafast Coherent Nuclear Motions of Hydrogen Bonded Carboxylic Acid Dimers. *Chem. Phys. Lett.* **2003**, *369*, 591−596.
(17) Heyne, K.; Huse, N.; Nibbering, E. T. J.; Elsaesser, T. Ultrafast Relaxation and Anharmonic Coupling of O-H Stretching and Bending Excitations in Cyclic Acetic Acid Dimers. *Chem. Phys. Lett.* **2003**, *382*, 19−25.
(18) Petersen, P. B.; Roberts, S. T.; Ramasesha, K.; Nocera, D. G.; Tokmakoff, A. Ultrafast N-H Vibrational Dynamics of Cyclic Doubly Hydrogen-Bonded Homo- and Heterodimers. *J. Phys. Chem. B* **2008**, *112*, 13167−13171.
(19) Van Hoozen, B. L., Jr.; Petersen, P. B. Origin of the 900 cm^{-1} Broad Double-Hump OH Vibrational Feature of Strongly Hydrogen-Bonded Carboxylic Acids. *J. Chem. Phys.* **2015**, *142*, 104308.
(20) Van Hoozen, B. L.; Petersen, P. B. A Combined Electronic Structure and Molecular Dynamics Approach to Computing the OH Vibrational Feature of Strongly Hydrogen-Bonded Carboxylic Acids. *J. Chem. Phys.* **2017**, *147*, 224304.
(21) Stingel, A. M.; Petersen, P. B. Couplings across the Vibrational Spectrum Caused by Strong Hydrogen Bonds: A Continuum 2D IR Study of the 7-Azaindole-Acetic Acid Heterodimer. *J. Phys. Chem. B* **2016**, *120*, 10768−10779.
(22) Heyne, K.; Huse, N.; Dreyer, J.; Nibbering, E. T. J.; Elsaesser, T.; Mukamel, S. Coherent Low-Frequency Motions of Hydrogen Bonded Acetic Acid Dimers in the Liquid Phase. *J. Chem. Phys.* **2004**, *121*, 902−913.
(23) Costard, R.; Greve, C.; Fidder, H.; Nibbering, E. T. J. Hydrogen Bonding Induced Enhancement of Fermi Resonances: Ultrafast Vibrational Energy Flow Dynamics in Aniline-d_5. *J. Phys. Chem. B* **2015**, *119*, 2711−2725.
(24) Van Hoozen, B. L., Jr.; Petersen, P. B. Origin of the Hadži ABC Structure: An Ab Initio Study. *J. Chem. Phys.* **2015**, *143*, 184305.
(25) Dahms, F.; Fingerhut, B. P.; Nibbering, E. T. J.; Pines, E.; Elsaesser, T. Large-Amplitude Transfer Motion of Hydrated Excess Protons Mapped by Ultrafast 2D IR Spectroscopy. *Science* **2017**, *357*, 491−495.
(26) Fournier, J. A.; Carpenter, W. B.; Lewis, N. H. C.; Tokmakoff, A. Broadband 2D IR Spectroscopy Reveals Dominant Asymmetric $H_5O_2^+$ Proton Hydration Structures in Acid Solutions. *Nat. Chem.* **2018**, *10*, 932−937.
(27) Yu, Q.; Carpenter, W. B.; Lewis, N. H. C.; Tokmakoff, A.; Bowman, J. M. High-Level VSCF/VCI Calculations Decode the Vibrational Spectrum of the Aqueous Proton. *J. Phys. Chem. B* **2019**, *123*, 7214−7224.
(28) Carpenter, W. B.; Yu, Q.; Hack, J. H.; Dereka, B.; Bowman, J. M.; Tokmakoff, A. Decoding the 2D IR Spectrum of the Aqueous Proton with High-Level VSCF/VCI Calculations. *J. Chem. Phys.* **2020**, *153*, 124506.
(29) Dereka, B.; Yu, Q.; Lewis, N. H. C.; Carpenter, W. B.; Bowman, J. M.; Tokmakoff, A. Crossover from Hydrogen to Chemical Bonding. *Science* **2021**, *371*, 160−164.
(30) Camerman, A.; Mastropaolo, D.; Camerman, N. Molecular Structure of Acetylacetone - A Crystallographic Determination. *J. Am. Chem. Soc.* **1983**, *105*, 1584−1586.
(31) Boese, R.; Antipin, M. Y.; Bläser, D.; Lyssenko, K. A. Molecular Crystal Structure of Acetylacetone at 210 and 110 K: Is the Crystal Disorder Static or Dynamic? *J. Phys. Chem. B* **1998**, *102*, 8654−8660.
(32) Srinivasan, R.; Feenstra, J. S.; Park, S. T.; Xu, S.; Zewail, A. H. Direct Determination of Hydrogen-Bonded Structures in Resonant and Tautomeric Reactions Using Ultrafast Electron Diffraction. *J. Am. Chem. Soc.* **2004**, *126*, 2266−2267.
(33) Caminati, W.; Grabow, J. U. The C_{2v} Structure of Enolic Acetylacetone. *J. Am. Chem. Soc.* **2006**, *128*, 854−857.
(34) Mavri, J.; Grdadolnik, J. Proton Potential in Acetylacetone. *J. Phys. Chem. A* **2001**, *105*, 2039−2044.
(35) Tayyari, S. F.; Milani-Nejad, F. Vibrational Assignment of Acetylacetone. *Spectrochim. Acta, Part A* **2000**, *56*, 2679−2691.
(36) Matanović, I.; Dočlić, N.; Mihalić, Z. Exploring the Potential Energy Surface for Proton Transfer in Acetylacetone. *Chem. Phys.* **2004**, *306*, 201−207.
(37) Broadbent, S. A.; Burns, L. A.; Chatterjee, C.; Vaccaro, P. H. Investigation of Electronic Structure and Proton Transfer in Ground State Acetylacetone. *Chem. Phys. Lett.* **2007**, *434*, 31−37.
(38) Howard, D. L.; Kjaergaard, H. G.; Huang, J.; Meuwly, M. Infrared and Near-Infrared Spectroscopy of Acetylacetone and Hexafluoroacetylacetone. *J. Phys. Chem. A* **2015**, *119*, 7980−7990.
(39) Käser, S.; Unke, O. T.; Meuwly, M. Reactive Dynamics and Spectroscopy of Hydrogen Transfer from Neural Network-Based Reactive Potential Energy Surfaces. *New J. Phys.* **2020**, *22*, No. 055002.
(40) Qu, C.; Conte, R.; Houston, P. L.; Bowman, J. M. Full-Dimensional Potential Energy Surface for Acetylacetone and Tunneling Splittings. *Phys. Chem. Chem. Phys.* **2021**, *23*, 7758−7767.
(41) Kaindl, R. A.; Wurm, M.; Reimann, K.; Hamm, P.; Weiner, A. M.; Woerner, M. Generation, Shaping, and Characterization of Intense Femtosecond Pulses Tunable from 3 to 20 μm. *J. Opt. Soc. Am. B* **2000**, *17*, 2086−2094.
(42) Helbing, J.; Hamm, P. Compact Implementation of Fourier Transform Two-Dimensional IR Spectroscopy without Phase Ambiguity. *J. Opt. Soc. Am. B* **2011**, *28*, 171.
(43) Mertz, L. Auxiliary Computation for Fourier Spectrometry. *Infrared Phys.* **1967**, *7*, 17−23.
(44) Gutiérrez-Quintanilla, A.; Chevalier, M.; Ceponkus, J.; Lozada-García, R. R.; Mestdagh, J. M.; Crépin, C. Large Amplitude Motions within Molecules Trapped in Solid Parahydrogen. *Faraday Discuss.* **2018**, *212*, 499−515.
(45) Frisch, M. J.; Trucks, G. W.; Schlegel, H. B.; Scuseria, G. E.; Robb, M. A.; Cheeseman, J. R.; Scalmani, G.; Barone, V.; Mennucci, B.; Petersson, G. A.; et al. *Gaussian 09*; Gaussian, Inc.: Wallingford, CT, USA, 2009.
(46) Johnson, C. J.; Dzugan, L. C.; Wolk, A. B.; Leavitt, C. M.; Fournier, J. A.; McCoy, A. B.; Johnson, M. A. Microhydration of Contact Ion Pairs in $M^{2+}OH^-(H_2O)_{n=1-5}$ (M = Mg, Ca) Clusters: Spectral Manifestations of a Mobile Proton Defect in the First Hydration Shell. *J. Phys. Chem. A* **2014**, *118*, 7590−7597.
(47) Blodgett, K. N.; Fischer, J. L.; Zwier, T. S.; Sibert, E. L., III The Missing NH Stretch Fundamental in S_1 Methyl Anthranilate: IR-UV Double Resonance Experiments and Local Mode Theory. *Phys. Chem. Chem. Phys.* **2020**, *22*, 14077−14087.
(48) Chen, L.; Fournier, J. A. Probing Hydrogen-Bonding Interactions within Phenol-Benzimidazole Proton-Coupled Electron Transfer Model Complexes with Cryogenic Ion Vibrational Spectroscopy. *J. Phys. Chem. A* **2021**, *125*, 9288−9297.
(49) Emsley, J.; Freeman, N. J. β-Diketone Interactions. Part 5. Solvent Effects on the Keto ⇋ Enol Equilibrium. *J. Mol. Struct.* **1987**, *161*, 193−204.
(50) Spencer, J. N.; Holmboe, E. S.; Kirshenbaum, M. R.; Firth, D. W.; Pinto, P. B. Solvent Effects on the Tautomeric Equilibrium of 2,4-Pentanedione. *Can. J. Chem.* **1982**, *60*, 1178−1182.
(51) Watarai, H.; Suzuki, N. Keto-Enol Tautomerization Rates of Acetylacetone in Water-Acetonitrile and Water-Dimethyl Sulfoxide Mixtures: Rate-Partition Relationship. *J. Inorg. Nucl. Chem.* **1976**, *38*, 1683−1686.
(52) Watarai, H.; Suzuki, N. Keto-Enol Tautomerization Rates of Acetylacetone in Mixed Aqueous-Media. *J. Inorg. Nucl. Chem.* **1974**, *36*, 1815−1820.

https://doi.org/10.1021/acs.jpcb.2c00793
J. Phys. Chem. B 2022, 126, 3551−3562

(53) Carpenter, W. B.; Fournier, J. A.; Biswas, R.; Voth, G. A.; Tokmakoff, A. Delocalization and Stretch-Bend Mixing of the HOH Bend in Liquid Water. *J. Chem. Phys.* **2017**, *147*, No. 084503.
(54) Hamm, P.; Zanni, M. T. *Concepts and Methods of 2D Infrared Spectroscopy*; Cambridge UP: Cambridge, 2011.
(55) Hamm, P.; Lim, M.; DeGrado, W. F.; Hochstrasser, R. M. Pump/Probe Self Heterodyned 2D Spectroscopy of Vibrational Transitions of a Small Globular Peptide. *J. Chem. Phys.* **2000**, *112*, 1907−1916.
(56) Khalil, M.; Demirdöven, N.; Tokmakoff, A. Vibrational Coherence Transfer Characterized with Fourier-Transform 2D IR Spectroscopy. *J. Chem. Phys.* **2004**, *121*, 362−373.
(57) Park, S.; Ji, M. Ultrafast Vibrational Population Transfer Dynamics in 2-Acetylcyclopentanone Studied by 2D IR Spectroscopy. *ChemPhysChem* **2011**, *12*, 799−805.
(58) De Marco, L.; Fournier, J. A.; Thämer, M.; Carpenter, W.; Tokmakoff, A. Anharmonic Exciton Dynamics and Energy Dissipation in Liquid Water from Two-Dimensional Infrared Spectroscopy. *J. Chem. Phys.* **2016**, *145*, 094501.
(59) Lock, A. J.; Woutersen, S.; Bakker, H. J. Ultrafast Energy Equilibration in Hydrogen-Bonded Liquids. *J. Phys. Chem. A* **2001**, *105*, 1238−1243.
(60) Lindner, J.; Vöhringer, P.; Pshenichnikov, M. S.; Cringus, D.; Wiersma, D. A.; Mostovoy, M. Vibrational Relaxation of Pure Liquid Water. *Chem. Phys. Lett.* **2006**, *421*, 563−567.
(61) Balasubramanian, M.; Reynolds, A.; Blair, T. J.; Khalil, M. Probing Ultrafast Vibrational Dynamics of Intramolecular Hydrogen Bonds with Broadband Infrared Pump-Probe Spectroscopy. *Chem. Phys.* **2019**, *519*, 38−44.
(62) Hamm, P.; Stock, G. Nonadiabatic Vibrational Dynamics in the HCO_2^-·H_2O Complex. *J. Chem. Phys.* **2015**, *143*, 134308.
(63) Myshakin, E. M.; Jordan, K. D.; Sibert, E. L., III; Johnson, M. A. Large Anharmonic Effects in the Infrared Spectra of the Symmetrical $CH_3NO_2^-$-H_2O and $CH_3CO_2^-$-H_2O Complexes. *J. Chem. Phys.* **2003**, *119*, 10138−10145.
(64) Relph, R. A.; Elliott, B. M.; Weddle, G. H.; Johnson, M. A.; Ding, J.; Jordan, K. D. Vibrationally Induced Interconversion of H-Bonded NO_2^-·H_2O Isomers within NO_2^-·H_2O·Ar_m Clusters Using IR-IR Pump-Probe through the OH and NO Stretching Vibrations. *J. Phys. Chem. A* **2009**, *113*, 975−981.
(65) Heine, N.; Kratz, E. G.; Bergmann, R.; Schofield, D. P.; Asmis, K. P.; Jordan, K. D.; McCoy, A. B. Vibrational Spectroscopy of the Water-Nitrate Complex in the O-H Stretching Region. *J. Phys. Chem. A* **2014**, *118*, 8188−8197.
(66) Zabuga, A. V.; Kamrath, M. Z.; Rizzo, T. R. Franck-Condon-Like Progressions in Infrared Spectra of Biological Molecules. *J. Phys. Chem. A* **2015**, *119*, 10494−10501.
(67) Liu, L.; Hunger, J.; Bakker, H. J. Energy Relaxation Dynamics of the Hydration Complex of Hydroxide. *J. Phys. Chem. A* **2011**, *115*, 14593−14598.
(68) Carpenter, W. B.; Fournier, J. A.; Lewis, N. H. C.; Tokmakoff, A. Picosecond Proton Transfer Kinetics in Water Revealed with Ultrafast IR Spectroscopy. *J. Phys. Chem. B* **2018**, *122*, 2792−2802.
(69) Ramasesha, K.; De Marco, L.; Mandal, A.; Tokmakoff, A. Water Vibrations Have Strongly Mixed Intra- and Intermolecular Character. *Nat. Chem.* **2013**, *5*, 935−940.
(70) Fournier, J. A.; Carpenter, W.; De Marco, L.; Tokmakoff, A. Interplay of Ion Water and Water Water Interactions within the Hydration Shells of Nitrate and Carbonate Directly Probed with 2D IR Spectroscopy. *J. Am. Chem. Soc.* **2016**, *138*, 9634−9645.
(71) Thøgersen, J.; Réhault, J.; Odelius, M.; Ogden, T.; Jena, N. K.; Jensen, S. J. K.; Keiding, S. R.; Helbing, J. Hydration Dynamics of Aqueous Nitrate. *J. Phys. Chem. B* **2013**, *117*, 3376−3388.
(72) Sturlaugson, A. L.; Fruchey, K. S.; Fayer, M. D. Orientational Dynamics of Room Temperature Ionic Liquid/Water Mixtures: Water-Induced Structure. *J. Phys. Chem. B* **2012**, *116*, 1777−1787.
(73) Sturlaugson, A. L.; Fruchey, K. S.; Lynch, S. R.; Aragón, S. R.; Fayer, M. D. Orientational and Translational Dynamics of Polyether/Water Solutions. *J. Phys. Chem. B* **2010**, *114*, 5350−5358.
(74) Giammanco, C. H.; Wong, D. B.; Fayer, M. D. Water Dynamics in Divalent and Monovalent Concentrated Salt Solutions. *J. Phys. Chem. B* **2012**, *116*, 13781−13792.
(75) Shirota, H. Intermolecular Vibrations and Diffusive Orientational Dynamics of C_s Condensed Ring Aromatic Molecular Liquids. *J. Phys. Chem. A* **2011**, *115*, 14262−14275.
(76) Verma, P. K.; Steinbacher, A.; Koch, F.; Nuernberger, P.; Brixner, T. Monitoring Ultrafast Intramolecular Proton Transfer Processes in an Unsymmetric β-Diketone. *Phys. Chem. Chem. Phys.* **2015**, *17*, 8459−8466.
(77) Baba, T.; Tanaka, T.; Morino, I.; Yamada, K. M. T.; Tanaka, K. Detection of the Tunneling-Rotation Transitions of Malonaldehyde in the Submillimeter-Wave Region. *J. Chem. Phys.* **1999**, *110*, 4131−4133.
(78) Lüttschwager, N. O. B.; Wassermann, T. N.; Coussan, S.; Suhm, M. A. Periodic Bond Breaking and Making in the Electronic Ground State on a Sub-Picosecond Timescale: OH Bending Spectroscopy of Malonaldehyde in the Frequency Domain at Low Temperature. *Phys. Chem. Chem. Phys.* **2010**, *12*, 8201−8207.

https://doi.org/10.1021/acs.jpcb.2c00793
J. Phys. Chem. B 2022, 126, 3551−3562